American Mineralogist, Volume 110, pages 1719–1727, 2025

High-energy resolution X-ray absorption spectroscopy study of the state of Pt in pyrite

Olga Filimonova[1,2,3,*,†], Elena Bazarkina[4,5,‡], Ruben Piña Garcia[6,§], Mauro Rovezzi[7,‖], and Didier Wermeille[1,2,#]

[1]The XMaS Beamline CRG c/o European Synchrotron Radiation Facility (ESRF), 71 avenue des Martyrs, 38000, Grenoble, France
[2]Department of Physics, University of Liverpool, Oliver Lodge Laboratory, L69 7ZE, Liverpool, U.K.
[3]European Synchrotron Radiation Facility (ESRF), 71 avenue des Martyrs, CS 40220, 38043, Grenoble, France
[4]The Rossendorf Beamline CRG c/o European Synchrotron Radiation Facility (ESRF), 71 avenue des Martyrs, 38000, Grenoble, France
[5]Institute of Resource Ecology, Helmholtz Zentrum Dresden-Rossendorf (HZDR), Bautzner Landstraße 400, 01328, Dresden, Germany
[6]Departamento de Mineralogía y Petrología, Universidad Complutense de Madrid, 28040, Madrid, Spain
[7]Université Grenoble Alpes, CNRS, IRD, Irstea, Météo France, OSUG, FAME, 38000, Grenoble, France

Abstract

Pyrite (FeS_2) is a common host mineral of Pt in many types of deposits of late magmatic and hydrothermal origin, including the Aguablanca Ni-Cu ore deposit in southwestern Spain. Yet the exact state of Pt in the pyrite from Aguablanca, including its oxidation state and local atomic geometry, still lacks spectroscopic evidence. Here, we investigated the state of ~30 ppm of Pt in a natural pyrite sample from Aguablanca using the high-energy resolution fluorescence detection X-ray absorption near edge structure (HERFD-XANES) technique. Our analysis of the Pt L_3-edge HERFD-XANES experimental spectra and theoretical spectra simulations performed via the ab initio FDMNES code revealed that Pt is incorporated in the cationic subshell of the natural pyrite sample. The presence of Pt-bearing micro- or nano-sized inclusions disseminated in the pyrite matrix was ruled out. The Pt-S interatomic distance ($R_{Pt\text{-}S}$) of 2.34 ± 0.01 Å in the Aguablanca sample is almost identical to that in the Pt-doped synthetic pyrite sample ($R_{Pt\text{-}S}$ = 2.35 ± 0.01 Å). The Pt-S interatomic distance is ~3.5% larger than the Fe-S interatomic distance in the pure pyrite structure, primarily due to a 3% difference between the covalent radii of Pt and Fe, rather than differences in their ionic radii or electronegativities. The Pt "formal" oxidation state of +3.5 and partial atomic charge of +0.4 e in the natural sample substantially exceed those of Fe in the pure pyrite structure (+2 and +0.2 e, respectively). By employing available literature data on the solubility of Pt in synthetic pyrite samples, we demonstrated that the Pt enrichment of the natural pyrite specimen took place at a temperature above 360 °C.

Keywords: Isomorphous platinum, solid solution, natural pyrite, HERFD-XAS, X-ray absorption spectroscopy, solubility, Ni-Cu-PGE Aguablanca ore deposit, Spectroscopy in Geology: A Decade of Breakthroughs

Introduction

Pyrite (FeS_2) is a typical carrier of the refractory, or so-called "invisible," form of Platinum Group Elements (PGEs) and Au. Pyrite can be enriched by as much as several hundred ppm of Pt in the deposits of orthomagmatic (e.g., Graham et al. 2017; Smith et al. 2014; Cabri et al. 2008; Oberthür et al. 1997), magmatic, and post-magmatic hydrothermal (e.g., Boucher et al. 2023; Robb et al. 2023; Piña et al. 2016, 2015, 2013; Duran et al. 2015; Djon, Barnes 2012; Gervilla and Kojonen 2002; Distler et al. 1999) origin. A review and analysis of the literature on the solubility of Pt in the pyrite samples are provided by Filimonova et al. (2019, 2022). Our previous study on the state of Pt in the samples of pyrite synthesized in the system saturated with respect to Pt was performed by X-ray absorption spectroscopy (XAS) (Filimonova et al. 2019) and demonstrated that both Pt solid solution and PtS_2 nano-sized inclusions (at high-Pt content) can enrich synthetic crystals of pyrite. Under the experimental conditions of that study, the content of Pt in solid solution reached ~0.25 wt% at 580 °C. The solubility of Pt in pyrite and pyrrhotite in the saturated systems was calculated based on the study of the synthetic Pt-doped crystals by Filimonova et al. (2022), based on their results and literature data (Majzlan et al. 2002; Makovicky et al. 1988).

For over two decades, several authors have described the presence of significant amounts of Pt in pyrites from Ni-Cu-PGE magmatic sulfide deposits (Junge et al. 2019; Piña et al. 2016; Duran et al. 2015; Smith et al. 2014; Dare et al. 2011; Oberthür et al. 1997). Pyrite is often a minor ore phase among sulfides forming these ore deposits (namely, pyrrhotite, pentlandite, and chalcopyrite). Nevertheless, pyrite is the only sulfide hosting detectable amounts of Pt. The ore assemblage of the examined natural pyrite sample from the Aguablanca Ni-Cu ore deposit, SW Spain,

* Corresponding author E-mail: olga.filimonova@esrf.fr Orcid https://orcid.org/0000-0001-5713-7890
† Special collection papers can be found online at our website in the Special Collection section.
‡ Orcid https://orcid.org/0000-0002-5445-2438
§ Orcid https://orcid.org/0000-0001-8202-7300
‖ Orcid https://orcid.org/0000-0003-2539-6198
Orcid https://orcid.org/0009-0007-8849-4226

0003-004X/25/0011–1719$05.00/DOI: https://doi.org/10.2138/am-2024-9596

exhibits this feature (Piña 2019, and references therein). The semi-massive ore mineralization of Aguablanca comprises large idiomorphic pyrite grains within pyrrhotite and pentlandite.

In the present study, we examined the pyrite grain, which was previously studied by the LA-ICP-MS method and contained up to 30 ppm of Pt (Piña et al. 2008, 2013). In this grain, the elevated Pt content was spatially related to high Co, Se, As, and Rh concentrations, but it was still unclear whether Pt occurred as nano-sized inclusions or a solid solution within the pyrite structure. To determine the state of ~30 ppm of Pt in the natural large idiomorphic pyrite crystal from the Ni-Cu-PGE Aguablanca ore deposit, we applied the XAS technique combined with the theoretical spectra modeling performed via the FDMNES code. The experimental Pt L_3-edge X-ray near-edge spectra (XANES, extending up to 50 eV above the absorption edge) were obtained in the high-energy resolution fluorescence detection (HERFD) mode to enhance spectral resolution and improve the signal-to-background ratio.

Considering that from the analytical point of view, the Pt content of 30 ppm disseminated within the pyrite structure is extremely low, HERFD-XANES is the only reliable method for Pt state characterization. The XANES region of the spectrum serves as a fingerprint of the local atomic environment surrounding the absorbing atom and its electronic structure (e.g., Mottana 2004). The use of the XAS method enabled the determination of the state of isomorphous Pt in the natural pyrite sample from the Ni-Cu-PGE Aguablanca ore deposit. The interpretation of the XANES region provided important information, including local atomic geometry, "formal" oxidation state, partial atomic charges of the absorbing atom, and the interatomic distances, coordination numbers, and types of neighboring atoms in the first coordination shell. Based on the new HERFD-XANES data and previous studies of Pt solubility in the synthetic pyrite samples, we estimated the temperature of the Pt enrichment of the natural pyrite specimen from the Ni-Cu-PGE Aguablanca ore deposit.

Methods

HERFD-XAS spectra acquisition and processing

Experimental spectra were recorded at the FAME-UHD beamline (BM16, Proux et al. 2017) of the European Synchrotron Radiation Facility (ESRF, Grenoble, France). High-energy resolution fluorescence detection X-ray absorption near edge structure (HERFD-XANES) spectra were recorded at the Pt L_3-edge. The ring current was 75 mA (16-bunch filling mode). The spot size was ~70 × 200 μm^2 (vertical × horizontal). The spectrometer was equipped with seven Ge(660) spherically bent crystal analyzers, each with a radius of curvature of 1 m, aligned to the Pt$L\alpha_1$ emission line (9442 eV) at a Bragg angle of 79.95°. An energy-resolving silicon drift diode (SDD) detector was used to increase the signal-to-background ratio. The sample, analyzer crystals, and detector were arranged in a vertical Rowland circle geometry. The incoming energy calibration was performed using the Pt L_3-edge XANES of Pt metallic foil, setting the first maximum of the first derivative to 11 564 eV. Fifteen energy scans of Pt disseminated in the natural pyrite specimen were recorded in the range from 11 540 to 11 700 eV and then averaged. The distribution of Pt was characterized by X-ray fluorescence mapping under a fixed incoming energy of 11 567.0 eV. The area of 2 × 2 mm was scanned with the steps of 50 μm in the vertical direction and 100 μm in the horizontal direction.

The natural sample was mounted in epoxy resin. Synthetic reference materials were powdered and spread on adhesive Kapton tape. The analyses of the HERFD-XANES spectra were performed using the Athena program of the software package IFEFFIT (Ravel and Newville 2005; Zabinsky et al. 1995). Data processing included energy calibration, determination of the position of the absorption edge (edge jump, e.j.), and the first intense feature (white line, WL), as well as background subtraction and normalization of the spectra.

FDMNES modeling of XANES spectra

Modeling of the HERFD-XANES spectra was performed via the ab initio FDMNES code (finite difference method for near-edge structure code) (Joly 2001; Guda et al. 2015). Relativistic calculations were performed with a 6 Å cluster radius and a 3 × 3 × 3 supercell non-relaxed structure. The parameters of simulation and convolution (*Gamma_hole* = 1.5 eV, E_{Fermi} = 0 eV; *Gamma_max* = 15 eV) optimized for the reference compound of PtS_2 (space group $P\bar{3}m$ and lattice parameters $a = b = 3.5432$, $c = 5.0388$ Å) (Grønvold et al. 1960) were used to simulate the HERFD-XANES spectra of the Pt-bearing pyrite sample (space group $Pa\bar{3}$ and lattice parameters $a = b = c = 5.4179$ Å) (Brostigen et al. 1969). Pt atom was introduced in the cationic site, and the Me-S interatomic distance in the first coordination shell was increased from 2.26 Å (Fe-S distance in the pure pyrite structure) to 2.31–2.39 Å [cf. the Pt-S distance of 2.35 Å obtained for the Pt-doped pyrite sample by Filimonova et al. (2019)]. The simulated HERFD-XANES spectra were compared to the experimental ones.

Determination of "formal" oxidation state and evaluation of partial atomic charges

The absorption edge position is sensitive to the local atomic symmetry and the oxidation state of the absorbing atom. The comparison of the experimental pyrite spectra with the spectra of reference materials with known oxidation states provides the value of the "formal" oxidation state of the absorbing atom. The use of the "formal" oxidation state concept suggests that the chemical bond in a compound is purely ionic. However, in the case of sulfides, the bonding Me-S is substantially covalent, and the partial atomic charge is different from the "formal" one. For this reason, two approaches were employed in this study to determine the oxidation state. First, the "formal" oxidation state of Pt in the natural sample of pyrite was determined through the comparison of the XANES spectrum of the natural pyrite with the spectra of the references. Second, the Bader and DDEC6 (density-derived electrostatic and chemical) partial atomic charges of Pt in the natural pyrite sample were determined from the empirical data using the calculated charges of Pt in Pt-bearing compounds following the procedure described by Evstigneeva et al. (2021).

Results and Discussion

Concentration and distribution of Pt in the natural pyrite sample

The large idiomorphic pyrite grain (~1.2 × 1.2 mm) examined in the present study was previously analyzed via LA-ICP-MS technique by Piña et al. (2013). According to their investigation, the pyrite grain contained up to 30 ppm of Pt in the most enriched central part of the grain, 10 ppm of Os, 20 ppm of Ir, 25 ppm of Ru, 100 ppm of Rh, 1 wt% of Co, 60 ppm of Se, and 1 wt% of As. Pt showed a similar spatial distribution compared to Co, Se, As, and Rh. The other elements—Bi, Te, Sb, Pd, and Au—were homogeneously distributed within the pyrite grain. The pyrite sample was free of micro-sized inclusions. The detailed analyses of LA-ICP-MS profiles and mapping revealed that the distribution of Pt was of zonal character with respect to the "intersections of Pt-rich bands oriented parallel to the grain boundaries" (Piña et al. 2013). Piña et al. (2013) suggested that the large idiomorphic pyrite grain located within pyrrhotite and pentlandite was formed as a result of the circulation of late magmatic/hydrothermal fluids that caused an increase in sulfur fugacity, resulting in the replacement of pyrrhotite by pyrite.

Pt L_3-edge HERFD-XANES spectra

This study provides the first HERFD-XANES spectrum of "invisible" Pt in the natural pyrite of semi-massive ore from the Aguablanca deposit. Our study confirms the advantages of the HERFD-XANES technique for Pt studies. The Pt L_3-edge XANES spectra of reference compounds with different

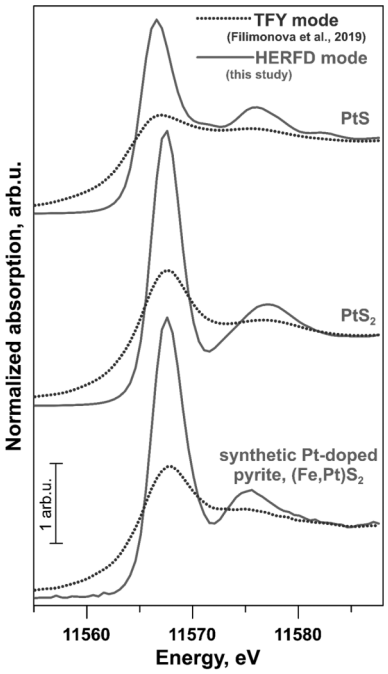

FIGURE 1. Comparison of Pt L_3-edge spectra of reference materials recorded in TFY (Filimonova et al. 2019) and HERFD modes (this study).

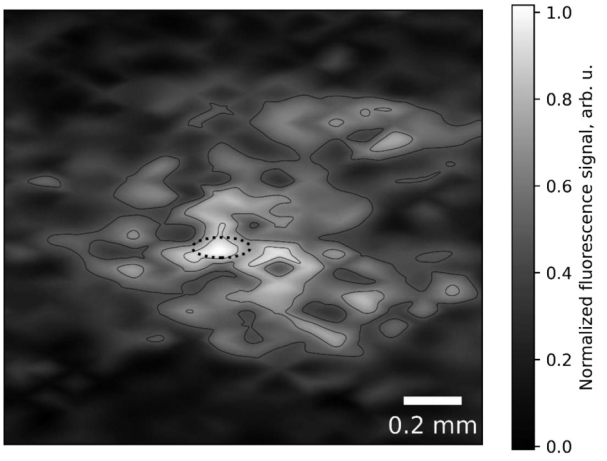

FIGURE 2. Map of the natural Pt-bearing grain of pyrite from Aguablanca Ni-Cu sulfide deposit performed at 11 567.0 eV incident beam energy. HERFD-XANES Pt L_3-edge spectrum was recorded in the zone of the maximum intensity of the Pt signal, denoted with the dotted ellipse.

structures and different oxidation states, recorded in total fluorescence yield mode (TFY) and HERFD modes, are compared in Figure 1. The main features of the HERFD-XANES spectra are more pronounced and better resolved compared to the standard-resolution XANES (TFY mode). The use of HERFD mode enabled the performance of a comprehensive analysis of the XANES spectrum of Pt in the natural sample. To visualize the Pt distribution in the grain of interest, we performed HERFD-based X-ray fluorescence mapping (Fig. 2). For the mapping, the incident energy was fixed at 11 567.0 eV and the intensity of the Pt signal was measured in the selected sample area. The HERFD-XANES spectra were recorded in the zone of the pyrite grain with the highest fluorescence signal. The HERFD-XANES spectra of the reference materials and natural sample are shown in Figure 3. PtS_{cr}, $PtAs_{2cr}$, $PtTe_{2cr}$, $PtSe_{2cr}$, PtS_{2cr}, and a synthetic Pt-doped pyrite sample containing 0.25 wt% of isomorphous Pt were used as the reference materials. Hereinafter, the isomorphous Pt in the pyrite structure will be referred to as $(Fe,Pt)S_{2cr}$. Positions of the absorption edges (edge jump, e.j.), and the first and second intense features (white line WL and peak B, respectively) are listed in Table 1.

Local atomic environment and geometry. The shape and main spectral features of the Pt-bearing natural pyrite spectrum are different from those of the spectra of metallic Pt, $Pt^{2+}S$, $Pt^{4+}As_2$, $Pt^{4+}Te_2$, and $Pt^{4+}Se_2$. This indicates that: (1) the local atomic environment of Pt in the sample of natural pyrite cannot be represented by S square- or As/Te/Se octahedron-coordination, and (2) Pt does not form Pt-Pt, Pt-Se, Pt-Te, or Pt-As bonds even though Piña et al. (2013) demonstrated that the central part of the grain enriched in Pt contained elevated concentrations of Se, Te, and As (Table 1; Fig. 3). The large intensity of the white line and the rightward energy shift of the main spectral features compared to that of Pt^0 and $Pt^{2+}S$ indicate that the presence of metallic Pt or its intermetallic compounds or PtS can be ruled out.

At the same time, the position and shape of the WLs of the spectra are close to those of Pt in $Pt^{4+}S_2$ and synthetic $(Fe,Pt)S_2$ (see Table 1). In these compounds, the local atomic environment of Pt consists of 6 S atoms (octahedron). The position of the second peak (i.e., peak B, Table 1) is different for the spectrum of Pt in PtS_2 and the spectra of Pt in both synthetic and natural pyrite samples. Thus, the presence of PtS_2 in the pyrite samples was ruled out. The spectrum of isomorphous Pt in the synthetic pyrite sample is almost identical to the spectrum of Pt in the sample of natural pyrite. Therefore, we conclude that Pt enriches the natural pyrite specimen as a solid solution.

As was determined for synthetic Pt-bearing pyrite crystals, Pt can additionally form nano-sized inclusions of PtS_2 and possibly PtS (Filimonova et al. 2019). However, the attempts to describe the XANES region of Pt in the natural sample by the combination of $(Fe,Pt)S_2$ and $PtS/PtS_2/PtSe_2/PtAs_2$ failed (detection limit of linear combination fit technique (LCF) ~5–10% (Bazarkina et al. 2010; Kelly et al. 2008). This also means that the Pt state is different from that in the reference materials. These analyses enable us to conclude that Pt is incorporated into the natural pyrite matrix as an isomorphous solid solution, without the formation of nano-sized inclusions. The formula of the studied grain of the natural pyrite can be written as $Pt_{0.002}Fe_{99.998}S_{200}$ (C_{Pt} = 30 ppmw = 0.185 ppma; ppma calculated for the stoichiometric pyrite composition).

"Formal" oxidation state. The intensity of WL of the spectra of Pt in the natural and synthetic pyrite samples is slightly lower than that of Pt in PtS_2. Although the L_3-edge XANES spectrum probes the $2p_{3/2} \rightarrow 5d_{3/2}$, $5d_{5/2}$ dipole transitions, the Pt L_3-edge spectrum reflects only the unoccupied $5d_{5/2}$. Hence, the area and intensity of the white line of the Pt L_3-edge spectrum are proportional to the number of vacancies in the *d* states (Lee et al. 2000; Mansour et al. 1984, and references therein). Thus, in the pyrite structure, the positive charge on

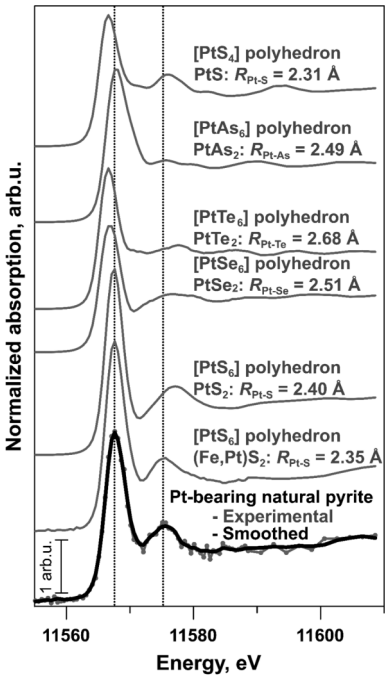

Figure 3. Pt L_3-edge HERFD-XANES normalized spectra of reference materials and natural Pt-bearing pyrite specimen. All experimental spectra are shown in gray. The smoothed spectrum of the natural sample is shown in black. The vertical dotted lines denote the main features typical of the spectrum of isomorphous Pt in pyrite structure $(Fe,Pt)S_2$. Pt-S/As/Se/Te interatomic distances are adopted from Rozhdestvina et al. (2008), Brostigen et al. (1969), Furuseth et al. (1965a, 1965b), and Grønvold et al. (1960).

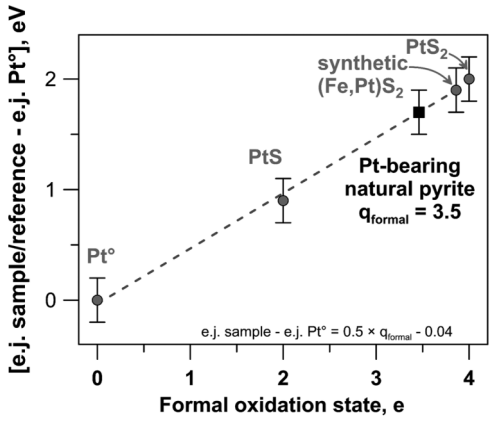

Figure 4. The difference between the positions of the absorption edges (e.j.) of sample/reference material and metallic Pt as a function of the "formal" oxidation state of Pt. The gray dashed line represents the regression through the values obtained for the reference materials, shown as gray circles. The calculated Pt "formal" oxidation state of +3.5 in the natural sample is plotted as a black square.

Table 2. Partial atomic charges of Pt in the references and natural pyrite sample

Sample ID	WL amplitude (±0.1)	DDEC6 charge of Pt, *e*	Bader charge of Pt, *e*
$PtSe_2$	6.7	+0.25[a]	+0.20[a]
PtS_2	10.4	+0.47[a]	+0.64[a]
Pt-bearing synthetic pyrite $(Pt,Fe)S_2$	9.6	+0.44[a]	+0.54[a]
Pt-bearing natural pyrite	8.7	+0.37	+0.44

[a] Data from Evstigneeva et al. (2021).

Pt is lower than that on Pt in PtS_2. To confirm this observation, the "formal" oxidation state of Pt in the pyrite sample was estimated through the e.j. positions. The difference between the e.j. of the spectra of the references of Pt^0, $Pt^{2+}S$, $Pt^{4+}S_2$, and the e.j. of the spectrum of metallic Pt is shown as a function of the "formal" oxidation state of Pt in Figure 4. According to this graph, the "formal" oxidation states of Pt in the synthetic and natural pyrite samples are +3.9 and +3.5, respectively, while the "formal" oxidation state of Fe in FeS_2 is +2.

Partial atomic Bader and DDEC6 charges. The data on calculated partial atomic Bader and DDEC6 charges on Pt in PtS_2, $PtSe_2$, and $(Pt,Fe)S_2$ are given in Table 2. To obtain a calibration curve, we calculated the area under the white line and plotted these data on a graph of the area under the first intense peak (WL) vs. the calculated DDEC6 and Bader charges (Figs. 5a and 5b, respectively). The regression lines through all the values for reference materials are shown as dashed lines. Partial atomic DDEC6 and Bader charges of Pt in the natural pyrite sample are +0.37 and +0.44 e, respectively. These values are slightly lower than those for the synthetic pyrite sample (+0.44 and +0.54 e, respectively). The DDEC6 charge of Fe is close to +0.18 e, and that of S is −0.11 e (Evstigneeva et al. 2021). This means that the partial atomic charges of Pt are 2–3 times higher than those of Fe. This result is consistent with that obtained for the "formal" oxidation state.

Table 1. The positions of the Pt L_3-edge HERFD-XANES features in the experimental spectra of the references and natural pyrite sample

Sample ID	Mineral analog	Energy position of the main features (±0.2 eV), eV[a]		
		e.j.	WL	Peak B
Pt^0	metallic Pt[b]	11564.0	11566.6	11580.5
$Pt^{2+}S$	cooperite	11564.9	11566.6	11576.0
$Pt^{4+}As_2$	sperrylite	11566.0	11567.8	11575.8
$Pt^{4+}Te_2$	moncheite	11564.9	11566.6	11577.5
$Pt^{4+}Se_2$	sudovikovite	11565.2	11567.0	11577.1
$Pt^{4+}S_2$	–	11566.0	11567.6	11576.8
Pt^{4+}-bearing synthetic pyrite $(Pt,Fe)S_2$	pyrite	11565.9	11567.6	11575.1
Pt-bearing natural pyrite	pyrite	11565.7	11567.5	11575.1

[a] Experimental spectra were calibrated with respect to the absorption edge of metallic Pt (11 564 eV); e.j. = edge jump, absorption edge; WL = white line, first intense peak; peak B = second intense peak.
[b] The spectrum of metallic Pt was recorded in the transmission mode.

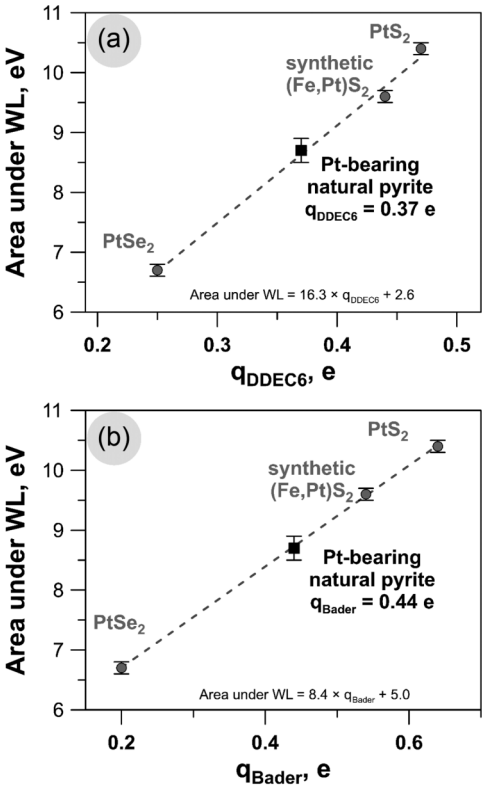

FIGURE 5. The area under the white line of the Pt L_3-edge HERFD-XANES spectra as a function of the partial atomic (**a**) DDEC6 and (**b**) Bader charges. The gray dashed lines correspond to the regression through the values obtained for the reference materials (gray circles). Calculated partial atomic DDEC6 and Bader charges of Pt in the natural sample are plotted as black squares.

Interatomic distance Pt-S in the first coordination shell. The spectrum of PtS_2, with its known local atomic structure and geometry (Grønvold et al. 1960), was used as a reference material. The experimental and FDMNES-simulated spectra of Pt in PtS_2 are given in Figure 6a. The parameters of simulation and convolution defined for Pt in PtS_2 were used for the calculations of the spectra of the Pt-bearing pyrite samples.

The set of simulations described below was aimed at determining the Pt-S interatomic distance in the first coordination shell in the natural pyrite specimen. The calculation results are shown in Figures 6b–6e and given in Table 3. The simulations were performed for five $R_{Pt\text{-}S}$ interatomic distances in the first coordination shell—2.31, 2.33, 2.35, 2.37, and 2.39 Å—of the pyrite structure (Brostigen et al. 1969). Simulated spectra are shown in varying shades of gray in Figure 6b. The increase in Pt-S interatomic distance leads to a rightward shift in the position of peak B and a leftward shift in the position of peak C, as indicated by the black arrows. The energy differences ΔE between positions of the WL and peak B/peak C for five models are presented as functions of the Pt-S distances in Figure 6c–6d. The values of Pt-S interatomic distances in natural and synthetic samples were calculated through the equations given in the figures. The calculated values are plotted in Figures 6c and 6d. The theoretical value of Pt-S interatomic distance in the synthetic pyrite sample of ~2.35 Å is identical to the value of 2.35 ± 0.01 Å defined for the same sample by EXAFS method in Filimonova et al. (2019). The calculated value of Pt-S interatomic distance in the spectrum of the natural sample is ~2.34 ± 0.01 Å. The spectra of Pt for both pyrite samples are shown together with one of the "best" FDMNES-simulated models with $R_{Pt\text{-}S}$ of 2.35 Å (Fig. 6e). The shape and positions of the main features of the experimental and modeled Pt-bearing pyrite spectra are close, indicating that Pt enriches the natural pyrite specimen as an isomorphous solid solution. The replacement of Fe by Pt increases the Me-S interatomic distance by 3.5% from $R_{Fe\text{-}S}$ = 2.26 Å (Brostigen et al. 1969) to $R_{Pt\text{-}S}$ = 2.34 ± 0.01 Å.

The percentage of ionic character of bonding in compounds can be determined according to the equation (Hannay and Smyth 1946; Pauling 1940):

$$\text{Percentage of ionic character} = 0.16 \times (\chi_{anion} - \chi_{cation}) + 0.035 \times (\chi_{anion} - \chi_{cation})^2 \quad (1)$$

The revisited values of average Pauling electronegativities (χ) for S, Fe, and Pt are 2.58, 1.83, and 2.28 electronegativity units, respectively (±0.1) (Allred 1961). Thus, using Equation 1, the percentages of covalent character for the Fe-S and Pt-S bonds are 86 and 95%, respectively. These values indicate that the bonding between Fe-S and Pt-S is predominantly covalent. Comparison of the revisited covalent radii of Fe (1.32 Å) and Pt (1.36 Å) (Cordero et al. 2008) suggests that in the case of the Pt isomorphic substitution, the increase in the interatomic distance of 3% should be observed. This value is in excellent agreement with the difference between Fe-S and Pt-S interatomic distances of 3.5%. This observation confirms the hypothesis proposed for synthetic Pt- and Pd-bearing pyrite crystals (Filimonova et al. 2024): the values of covalent radii control the incorporation of Pt atoms into the Fe sites of the pyrite structure. The increase in Me-S distance cannot be accounted for by the difference in the values of electronegativities or the difference in the ionic radii (Shannon 1976) of Pt and Fe.

Pyrite saturation with respect to Pt

Previous studies of the Aguablanca Ni-Cu-PGE deposit showed that the most typical ore mineral association consists of pyrrhotite + pentlandite + chalcopyrite ± pyrite ($po + pn + cp \pm py$; Ortega et al. 2004; Piña et al. 2008, 2013). The Fe–FeS, $Fe_{1-x}S$ – FeS_2, Pt – PtS, PtS – PtS_2, pyrite + bornite – chalcopyrite ($py + bn - cp$) equilibrium lines are plotted in the sulfur fugacity log f_{S_2} vs. reciprocal temperature 1000/T (Toulmin and Barton 1964) diagram (Fig. 7). Filimonova et al. (2022) studied the solubility of Pt in pyrite crystals and found that Pt solubility strongly depends on the 1000/T and log f_{S_2}. Using the results of their study, we added two fields of Pt solubility in pyrite: <10 and >10 ppm. In the case of the pyrite specimen from Aguablanca, roughly >10 ppm of

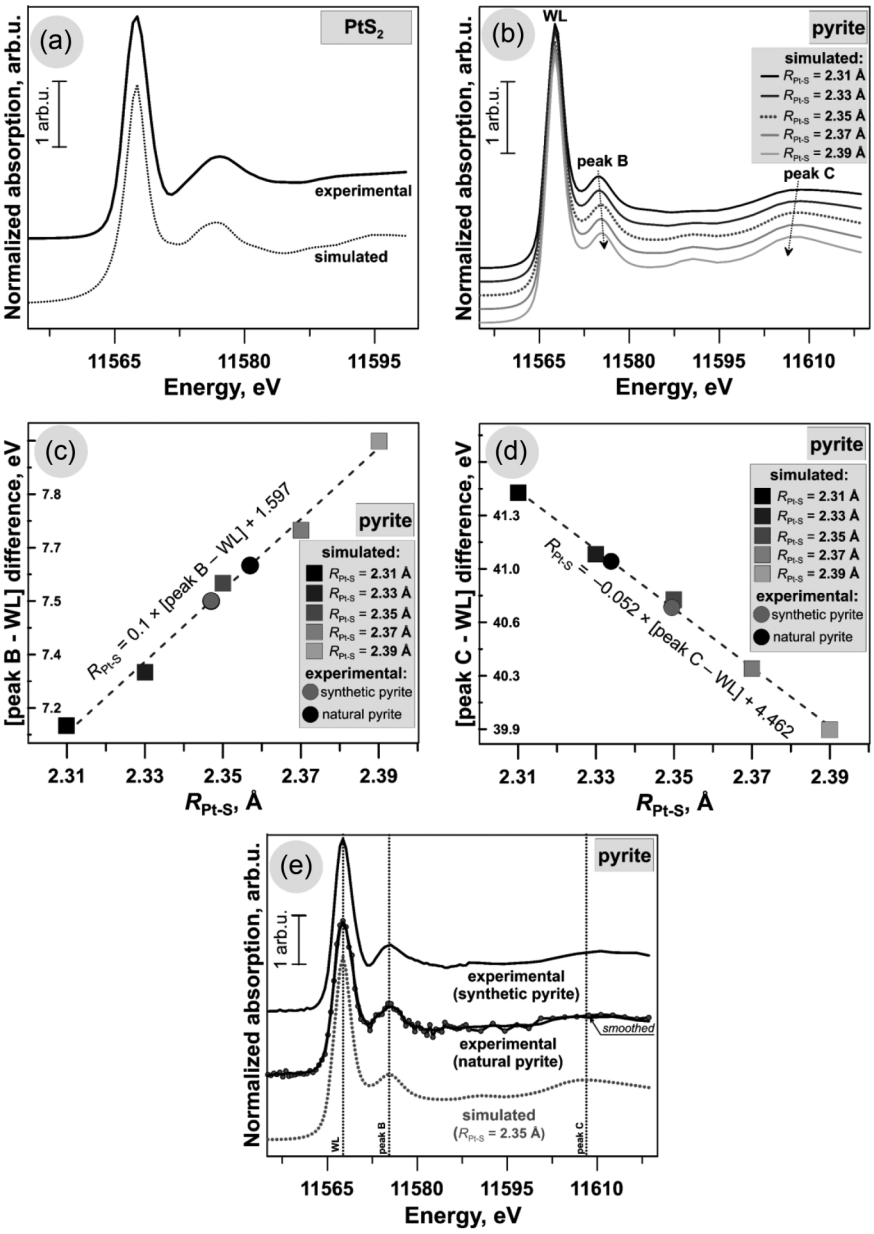

Figure 6. (**a**) Experimental Pt L_3-edge HERFD-XANES spectrum of synthetic PtS_2 (solid line) and simulated spectrum of PtS_2 (dotted line); (**b**) FDMNES-simulated XANES spectra of pyrite containing isomorphous Pt in the cation site. Simulated spectra were calculated for the models with the different Pt-S interatomic distances (2.31–2.39 Å). Dashed arrows denote the shifts of peaks B and C with the increase of $R_{Pt\text{-}S}$. For all the calculations, the energy origin is defined relative to the theoretical Fermi level; (**c**, **d**) The difference between the positions of peak B/C and WL (eV) as a function of the Pt-S interatomic distance (Å). The values defined from the simulated data are shown in gray squares. The values for the experimental data are shown in gray and black circles for the Pt-bearing synthetic and natural pyrite samples, respectively. The best agreement between the experimental and simulated data is obtained when Pt is surrounded by S atoms at 2.34–2.35 Å; (**e**) HERFD-XANES spectra of solid solution Pt in synthetic and natural pyrite samples $(Fe,Pt)S_2$. The best simulation of the XANES is archived when Pt is octahedrally coordinated by 6 S atoms at a distance of ~2.35 Å (dotted line). Vertical black dotted lines denote the positions of the main features in the Pt spectra of the natural and synthetic pyrite samples.

isomorphous Pt can be dissolved in the pyrite structure at sulfur fugacity log f_{S_2} of above –5.5 and temperature of 360 – 743 °C (but not at $T < 360$ °C). In this case, the temperature of 360 °C was "the minimal enrichment temperature" at which a pyrite grain containing ~30 ppm of the isomorphous Pt could be formed. This assessment is in excellent agreement with the model proposed by Piña et al. (2013), where large idiomorphic secondary pyrite grains mostly hosted by pyrrhotite and pentlandite were formed due to the increase of sulfur fugacity through the circulation of late magmatic/hydrothermal fluids.

Table 3. The FDMNES simulations of Pt local atomic coordination of studied pyrite samples determined for Pt L_3-edge HERFD-XANES spectra

Sample ID/Simulation	$R_{Pt\text{-}S}$, Å	Difference between peak B and WL, eV	Difference between peak C and WL, eV	Calculated $R_{Pt\text{-}S}$, Å		
				Equation 1, Figure 6e	Equation 2, Figure 6d	Average
Pt-bearing synthetic pyrite (Pt,Fe)S_2	2.35 ± 0.01[a]	7.50	40.70	2.35	2.35	2.35
Pt-bearing natural pyrite	–	7.60	41.00	2.36	2.33	2.34
Simulation 1	2.31	7.15	41.45	2.31	2.31	–
Simulation 2	2.33	7.30	41.05	2.33	2.33	–
Simulation 3	2.35	7.55	40.75	2.35	2.35	–
Simulation 4	2.37	7.70	40.30	2.37	2.37	–
Simulation 5	2.39	7.95	39.90	2.39	2.39	–

[a] $R_{Pt\text{-}S}$ predetermined using EXAFS spectrum fitting by Filimonova et al. (2019).

Concluding Remarks and Implications

We studied the state of Pt in a natural pyrite specimen from the Ni-Cu-PGE sulfide Aguablanca ore deposit by X-ray absorption spectroscopy at the Pt L_3-edge. From the point of view of XAS analysis, this pyrite sample containing ~30 ppm of Pt is extremely diluted; therefore, we applied the HERFD-XANES technique, which enables the recording of spectra with more pronounced and better-resolved peaks (Proux et al. 2017). Our study emphasizes the importance of using the HERFD mode for the precise and unambiguous identification of the state of PGEs in mineral matrices (e.g., Pokrovski et al. 2021; Trigub et al. 2017). A comparison of the shape and main features of the HERFD-XANES spectra of the Pt-bearing pyrite and reference materials showed that Pt forms an isomorphous solid solution substituting Fe in the pyrite cationic subshell. The presence of 1 wt% of As, 60 ppm of Se, and other admixtures does not affect the state of Pt in the pyrite structure. The formation of the second form of Pt, such as nano- or micro-sized inclusions of PtS_2, PtS, Pt metallic and intermetallic compounds, etc., described earlier in the synthetic pyrite samples (Filimonova et al. 2019) and other natural sulfides (e.g., Helmy et al. 2023; González-Jiménez et al. 2019, and references therein) was ruled out due to the identical shape and the positions of the main features of the HERFD-XANES spectra of Pt in the natural and synthetic pyrite samples.

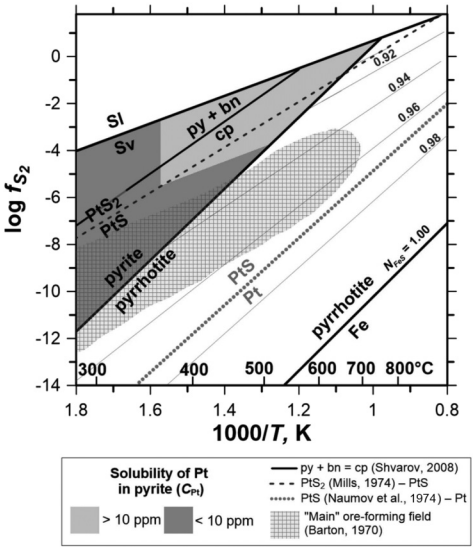

Figure 7. The solubility of Pt in pyrite as a function of sulfur fugacity log f_{S_2} and reciprocal temperature 1000/T. Data for the Fe-S system are adopted from Toulmin and Barton (1964). S_l refers to liquid sulfur, S_v to sulfur vapor. Filled gray fields correspond to the level of solubility of Pt in pyrite; data on solubility were adopted from Filimonova et al. (2022). According to this diagram, the natural pyrite sample from the Aguablanca deposit containing 30 ppm of isomorphous Pt was formed at a temperature of more than 360 °C and $-5.5 < \log f_{S_2} < 0.4$ (a light gray field, $C_{Pt} > 10$ ppm).

The "formal" oxidation state of isomorphous Pt in natural $Fe^{2+}S_2$ is close to +3.5. The partial atomic Bader and DDEC6 charges of Pt are ~+0.4 e (DDEC6 charge of Fe in the pure pyrite structure is ~+0.2 e, Evstigneeva et al. 2021). The estimations of the "formal" oxidation state, and partial atomic Bader and DDEC6 charges suggest that in the pyrite matrix, the overall valence electron density shifts away from the Pt atom. The values of "formal" oxidation states and partial atomic charges of Pt in the synthetic (0.25 wt%) and natural (~30 ppm) pyrite samples are identical within each category, regardless of the Pt concentration. The knowledge of the oxidation state of Pt in the pyrite structure can be used in the development of sustainable PGE leaching and extraction technologies.

To determine the Pt-S interatomic distance in the first coordination shell of the natural sample, simulations via FDMNES code were performed. The best convergence between the XANES spectrum of isomorphous Pt and the simulated one was achieved for the model where Pt substituted Fe in the cationic subshell, and the Pt-S interatomic distance was close to ~2.34–2.35 Å (cf. Fe-S interatomic distance is close to 2.26 Å) (Brostigen et al. 1969). The calculation of the percentage of the ionic character for Pt-S and Fe-S bonds suggests that both of them are strongly covalent (>85%) (Hannay and Smyth 1946; Pauling 1940). The difference between the covalent radii of Fe and Pt (Cordero et al. 2008) of 3% is close to the difference between the Fe-S and Pt-S bond distances of 3.5%. This observation: (1) demonstrates that the difference in covalent radii is more likely to control the incorporation of the Pt atom into the Fe position in the pyrite structure rather than the difference in ionic radii or electronegativities (cf. Filimonova et al. 2024), and, therefore, (2) contributes to the understanding of the PGE incorporation process into sulfide matrices from a crystallographic perspective.

Based on the literature data on Pt solubility in the synthetic and natural pyrite samples (Filimonova et al. 2022; Mironov et al. 2008; Large et al. 2007; Majzlan et al. 2002; Makovicky et al. 1992), we estimated the conditions at which the pyrite sample from the Aguablanca deposit was enriched with Pt. The sample was enriched by a few tens of ppm of Pt at $T > 360$ °C (minimal temperature of the enrichment) and

$f_{S_2} > -5.5$. This approach can be extended to determining the minimum temperature required for the formation of Pt-bearing pyrites from various deposits. The results of this study elucidate the important role of pyrite as a carrier of the isomorphous form of Pt in the Ni-Cu-PGE sulfide ore deposits.

Data availability

Data is available in the Online Materials[1].

Acknowledgments and Funding

The authors thank the European Synchrotron Radiation Facility (ESRF) for the beamtime allocation under proposal No. ES-1269 (BM16-FAME-UHD). We also acknowledge the XMaS/BM28 beamline, funded as a U.K. EPSRC National Research Facility located at the ESRF. The valuable comments and suggestions from the two anonymous reviewers and Associate Editor Fabrizio Nestola are greatly appreciated.

References Cited

Allred, A.L. (1961) Electronegativity values from thermochemical data. Journal of Inorganic and Nuclear Chemistry, 17, 215–221, https://doi.org/10.1016/0022-1902(61)80142-5.

Barton, P. (1970) Sulfide petrology. Mineralogical Society of America Special Paper, 3, 187–198.

Bazarkina, E.F., Pokrovski, G.S., Zotov, A.V., and Hazemann, J.L. (2010) Structure and stability of cadmium chloride complexes in hydrothermal fluids. Chemical Geology, 276, 1–17, https://doi.org/10.1016/j.chemgeo.2010.03.006.

Boucher, B.M., Robb, S.J., Hanley, J.J., Kerr, M.J., and Mungall, J.E. (2023) Platinum-group elements (PGE) in the New Afton alkalic Cu-Au porphyry deposit, Canadian Cordillera, I: Relationships between PGE, accessory metals and sulfur isotopes in pyrite. Frontiers in Earth Science (Lausanne), 11, 819129, https://doi.org/10.3389/feart.2023.819129.

Brostigen, G., Kjekshus, A., Astrup, E.E., Nordal, V., Lindberg, A.A., and Craig, J.C. (1969) Redetermined crystal structure of FeS_2 pyrite. Acta Chemica Scandinavica (Copenhagen, Denmark), 23, 2186–2188, https://doi.org/10.3891/acta.chem.scand.23-2186.

Cabri, L.J., Rudashevsky, N.S., and Rudashevsky, V.N. (2008) Current approaches for the process mineralogy of platinum-group element ores and tailings. Ninth Annual International Congress for Applied Mineralogy, p. 9–17.

Cordero, B., Gómez, V., Platero-Prats, A.E., Revés, M., Echeverría, J., Cremades, E., Barragán, F., and Alvarez, S. (2008) Covalent radii revisited. Dalton Transactions: An International Journal of Inorganic Chemistry, 21, 2832–2838, https://doi.org/10.1039/b801115j.

Dare, S.A., Barnes, S.J., Prichard, H.M., and Fisher, P.C. (2011) Chalcophile and platinum-group element (PGE) concentrations in the sulfide minerals from the McCreedy East deposit, Sudbury, Canada, and the origin of PGE in pyrite. Mineralium Deposita, 46, 381–407, https://doi.org/10.1007/s00126-011-0336-9.

Distler, V.V., Sluzhenikin, S.F., Krivolutskaya, N.A., Turovtsev, D.M., Golovanova, T.A., Mokhov, A.V., Cabri, L.J., Knauf, V.V., and Oleshkevich, O.I. (1999) Platinum ores of the Noril'sk layered intrusions: Magmatic and fluid concentration of noble metals. Geology of Ore Deposits, 41, 214–237.

Djon, M.L.N. and Barnes, S.J. (2012) Changes in sulfides and platinum-group minerals with the degree of alteration in the Roby, Twilight, and High Grade Zones of the Lac des Iles Complex, Ontario, Canada. Mineralium Deposita, 47, 875–896, https://doi.org/10.1007/s00126-012-0401-z.

Duran, C.J., Barnes, S.J., and Corkery, J.T. (2015) Chalcophile and platinum-group element distribution in pyrites from the sulfide-rich pods of the Lac des Iles Pd deposits, Western Ontario, Canada: Implications for post-cumulus re-equilibration of the ore and the use of pyrite compositions in exploration. Journal of Geochemical Exploration, 158, 223–242, https://doi.org/10.1016/j.gexplo.2015.08.002.

Evstigneeva, P.V., Trigub, A.L., Chareev, D.A., Nickolsky, M.S., and Tagirov, B.R. (2021) The charge state of Pt in binary compounds and synthetic minerals determined by X-ray absorption spectroscopy and quantum chemical calculations. Minerals, 11, 79, https://doi.org/10.3390/min11010079.

Filimonova, O.N., Nickolsky, M.S., Trigub, A.L., Chareev, D.A., Kvashnina, K.O., Kovalchuk, E.V., Vikentyev, I.V., and Tagirov, B.R. (2019) The state of platinum in pyrite studied by X-ray absorption spectroscopy of synthetic crystals. Economic Geology and the Bulletin of the Society of Economic Geologists, 114, 1649–1663, https://doi.org/10.5382/econgeo.4686.

Filimonova, O.N., Akinfiev, N.N., Abramova, V.D., Kovalchuk, E.V., Chareev, D.A., and Tagirov, B.R. (2022) Solubility of Platinum in Pyrite and Pyrrhotite. Geology of Ore Deposits, 64, 377–388, https://doi.org/10.1134/S1075701522060046.

Filimonova, O.N., Snigireva, I.I., Thompson, P., and Wermeille, D. (2024) Incorporation of palladium into pyrite: Insights from X-ray absorption spectroscopy analysis and modelling. The Science of the Total Environment, 920, 170927, https://doi.org/10.1016/j.scitotenv.2024.170927.

Furuseth, S., Selte, K., Kjekshus, A., Nielsen, P.H., Sjöberg, B., and Larsen, E. (1965a) Redetermined crystal structures of $PdAs_2$, $PdSb_2$, PtP_2, $PtAs_2$, $PtSb_2$, a-$PtBi_2$, and $AuSb_2$. Acta Chemica Scandinavica (Copenhagen, Denmark), 19, 735–741, https://doi.org/10.3891/acta.chem.scand.19-0735.

Furuseth, S., Selte, K., Kjekshus, A., Gronowitz, S., Hoffman, R.A., and Westerdahl, A. (1965b) Redetermined Crystal Structures of $NiTe_2$, $PdTe_2$, PtS_2, $PtSe_2$, and $PtTe_2$. Acta Chemica Scandinavica (Copenhagen, Denmark), 19, 257–258, https://doi.org/10.3891/acta.chem.scand.19-0257.

Gervilla, F. and Kojonen, K. (2002) The platinum-group minerals in the upper section of the Keivitsansarvi Ni-Cu-PGE deposit, northern Finland. Canadian Mineralogist, 40, 377–394, https://doi.org/10.2113/gscanmin.40.2.377.

González-Jiménez, J.M., Roqué-Rosell, J., Jiménez-Franco, A., Tassara, S., Nieto, F., Gervilla, F., Baurier, S., Proenza, J.A., Saunders, E., Deditius, A.P., and others. (2019) Magmatic platinum nanoparticles in metasomatic silicate glasses and sulfides from Patagonian mantle xenoliths. Contributions to Mineralogy and Petrology, 174, 47, https://doi.org/10.1007/s00410-019-1583-5.

Graham, S.D., Holwell, D.A., McDonald, I., Jenkin, G.R.T., Hill, N.J., Boyce, A.J., Smith, J., and Sangster, C. (2017) Magmatic Cu-Ni-PGE-Au sulphide mineralisation in alkaline igneous systems: An example from the Sron Garbh intrusion, Tyndrum, Scotland. Ore Geology Reviews, 80, 961–984, https://doi.org/10.1016/j.oregeorev.2016.08.031.

Grønvold, F., Haraldsen, H., Kjekshus, A., and Söderquist, R. (1960) On the sulfides, selenides and tellurides of platinum. Acta Chemica Scandinavica (Copenhagen, Denmark), 14, 1879–1893, https://doi.org/10.3891/acta.chem.scand.14-1879.

Guda, S.A., Guda, A.A., Soldatov, M.A., Lomachenko, K.A., Bugaev, A.L., Lamberti, C., Gawelda, W., Bressler, C., Smolentsev, G., Soldatov, A.V., and others. (2015) Optimized finite difference method for the full-potential XANES simulations: Application to molecular adsorption geometries in MOFs and metal-ligand intersystem crossing transients. Journal of Chemical Theory and Computation, 11, 4512–4521, https://doi.org/10.1021/acs.jctc.5b00327.

Hannay, N.B. and Smyth, C.P. (1946) The dipole moment of hydrogen fluoride and the ionic character of bonds. Journal of the American Chemical Society, 68, 171–173, https://doi.org/10.1021/ja01206a003.

Helmy, H.M., Botcharnikov, R., Ballhaus, C., Wirth, R., Schreiber, A., and Buhre, S. (2023) How Pt and Pd are hosted in magmatic sulfides, substitutions and/or inclusions? Contributions to Mineralogy and Petrology, 178, 41, https://doi.org/10.1007/s00410-023-02018-8.

Joly, Y. (2001) X-ray absorption near-edge structure calculations beyond the muffin-tin approximation. Physical Review B: Condensed Matter, 63, 125120, https://doi.org/10.1103/PhysRevB.63.125120.

Junge, M., Oberthür, T., Kraemer, D., Melcher, F., Piña, R., Derrey, I.T., Manyeruke, T., and Strauss, H. (2019) Distribution of platinum-group elements in pristine and near-surface oxidized Platreef ore and the variation along strike, northern Bushveld Complex, South Africa. Mineralium Deposita, 54, 885–912, https://doi.org/10.1007/s00126-018-0848-7.

Kelly, S.D., Hesterberg, D., Ravel, B. (2008) Analysis of soils and minerals using X-ray absorption spectroscopy. In A.L. Ulery and L.R. Drees, Eds., Methods of Soil Analysis Part 5—Mineralogical Methods, 5.5, p. 387–463. Soil Science Society of America, Inc.

Large, R.R., Maslennikov, V.V., Robert, F., Danyushevsky, L.V., and Chang, Z. (2007) Multistage sedimentary and metamorphic origin of pyrite and gold in the giant Sukhoi Log deposit, Lena gold province, Russia. Economic Geology and the Bulletin of the Society of Economic Geologists, 102, 1233–1267, https://doi.org/10.2113/gsecongeo.102.7.1233.

Lee, Y.S., Lim, K.Y., Chung, Y.D., Whang, C.N., and Jeon, Y. (2000) XPS core-level shifts and XANES studies of Cu-Pt and Co-Pt alloys. Surface and Interface Analysis, 30, 475–478, https://doi.org/10.1002/1096-9918(200008)30:1<475:AID-SIA817>3.0.CO;2-W.

Majzlan, J., Makovicky, M., Makovicky, E., and Rose-Hansen, J. (2002) The system Fe-Pt-S at 1100 °C. Canadian Mineralogist, 40, 509–517, https://doi.org/10.2113/gscanmin.40.2.509.

Makovicky M., Makovicky E., and Rose-Hansen J. (1988) Experimental evidence on the formation and mineralogy of platinum and palladium ore deposits. In J. Boissonnas and P. Omenetto, Eds., Mineral Deposits Within the European Community, p. 303–317. Springer.

Makovicky, M., Makovicky, E., and Rose-Hansen, J. (1992) The phase system Pt-Fe-As-S at 850 °C and 470 °C. Neues Jahrbuch für Mineralogie Monatshefte, 10, 441–453.

Mansour, A.N., Cook, J.W. Jr., and Sayers, D.E. (1984) Quantitative technique for the determination of the number of unoccupied d-electron states in a platinum catalyst using the $L_{2,3}$ X-ray absorption edge spectra. Journal of Physical Chemistry, 88, 2330–2334, https://doi.org/10.1021/j150655a029.

Mills, K.C. (1974) Thermodynamic Data for Inorganic Sulphides, Selenides and Tellurides, 845 p. Butterworths.

Mironov, A.G., Zhmodik, S.M., Kolesov, G.M., Mit'kin, V.N., Damdinov, B.B., and Zayakina, S.B. (2008) Platinum group elements in gold-sulfide and base-metal ores of the Sayan-Baikal fold region and possible platinum and palladium speciation in sulphides. Geology of Ore Deposits, 50, 41–59, https://doi.org/10.1134/S1075701508010029.

Mottana, A. (2004) X-ray absorption spectroscopy in mineralogy: Theory and experiment in the XANES region. In A. Beran and E. Libowitzky, Eds., EMU Notes in Mineralogy 6: Spectroscopic Methods in Mineralogy, p. 465–522. Mineralogical Society of Great Britain and Ireland.

Naumov, G.B., Ryzhenko, B.N., and Khodakovsky, I.L. (1974) Handbook of Thermodynamic Data, 328 p. U.S. Geological Survey, Water Resources Division.

Oberthür, T., Cabri, L.J., Weiser, T.W., McMahon, G., and Müller, P. (1997) Pt, Pd and other trace elements in sulfides of the main sulfide zone, Great Dyke, Zimbabwe: A reconnaissance study. Canadian Mineralogist, 35, 597–609.

Ortega, L., Lunar, R., García-Palomero, F., Moreno, T., Martín-Estévez, J.R., Prichard, H.M., and Fisher, P.C. (2004) The Aguablanca Ni-Cu-PGE deposit, southwestern Iberia: Magmatic ore-forming processes and retrograde evolution. Canadian Mineralogist, 42, 325–350, https://doi.org/10.2113/gscanmin.42.2.325.

Pauling, L. (1940) The electronic structure of atoms and the formal rules for the formation of covalent bonds. In The Nature of the Chemical Bond, 2nd edition, 664 p. Oxford University Press/Cornell University Press.

Piña, R. (2019) The Ni-Cu-(PGE) Aguablanca Ore Deposit (SW Spain). Springer Briefs in World Mineral Deposits.

Piña, R., Gervilla, F., Ortega, L., and Lunar, R. (2008) Mineralogy and geochemistry of platinum-group elements in the Aguablanca Ni-Cu deposit (SW Spain). Mineralogy and Petrology, 92, 259–282, https://doi.org/10.1007/s00710-007-0195-3.

Piña, R., Gervilla, F., Barnes, S.J., Ortega, L., and Lunar, R. (2013) Platinum-group elements-bearing pyrite from the Aguablanca Ni-Cu sulphide deposit (SW Spain): A LA-ICP-MS study. European Journal of Mineralogy, 25, 241–252, https://doi.org/10.1127/0935-1221/2013/0025-2290.

Piña, R., Gervilla, F., Barnes, S.J., Oberthür, T., Lunar, R. (2015) Platinum-group element abundances in pyrite from the main sulfide zone, Great Dyke, Zimbabwe, p. 971–974. Extended abstracts in the proceedings of the 13th Biennial Meeting of the Society for Geology Applied to Mineral Deposits, Nancy, France.

Piña, R., Gervilla, F., Barnes, S.J., Oberthür, T., and Lunar, R. (2016) Platinum-group element concentrations in pyrite from the main sulfide zone of the Great Dyke of Zimbabwe. Mineralium Deposita, 51, 853–872, https://doi.org/10.1007/s00126-016-0642-3.

Pokrovski, G.S., Escoda, C., Blanchard, M., Testemale, D., Hazemann, J.L.F., Gouy, S., Kokh, M.A., Boiron, M.C., De Parseval, F., Aigouy, T., and others. (2021) An arsenic-driven pump for invisible gold in hydrothermal systems. Geochemical Perspectives Letters, 17, 39–44, https://doi.org/10.7185/geochemlet.2112.

Proux, O., Lahera, E., Del Net, W., Kieffer, I., Rovezzi, M., Testemale, D., Irar, M., Thomas, S., Aguilar-Tapia, A., Bazarkina, E.F., and others. (2017) High-energy resolution fluorescence detected X-ray absorption spectroscopy: A powerful new structural tool in environmental biogeochemistry sciences. Journal of Environmental Quality, 46, 1146–1157, https://doi.org/10.2134/jeq2017.01.0023.

Ravel, B. and Newville, M. (2005) ATHENA, ARTEMIS, HEPHAESTUS: Data analysis for X-ray absorption spectroscopy using IFEFFIT. Journal of Synchrotron Radiation, 12, 537–541, https://doi.org/10.1107/S0909049505012719.

Robb, S.J., Boucher, B.M., Mungall, J.E., and Hanley, J.J. (2023) Platinum-group elements (PGE) in the New Afton alkalic Cu-Au porphyry deposit, Canadian Cordillera, II: PGE distribution and models for the hydrothermal coprecipitation of Co-Ni-Pd-Pt in pyrite. Frontiers in Earth Science (Lausanne), 11, 819109, https://doi.org/10.3389/feart.2023.819109.

Rozhdestvina, V.I., Ivanov, A.V., Zaremba, M.A., Antsutkin, O.N., and Forsling, W. (2008) Single-crystalline cooperite (PtS): Crystal-chemical characterization, ESR spectroscopy, and ^{195}Pt NMR spectroscopy. Crystallography Reports, 53, 391–397, https://doi.org/10.1134/S106377450803005X.

Shannon, R.D. (1976) Revised effective ionic radii and systematic studies of interatomic distances in halides and chalcogenides. Acta Crystallographica Section A, 32(5), 751–767, https://doi.org/10.1107/S0567739476001551.

Shvarov, Y.V. (2008) HCh: New potentialities for the thermodynamic simulation of geochemical systems offered by Windows. Geochemistry International, 46, 834–839, https://doi.org/10.1134/S0016702908080089.

Smith, J.W., Holwell, D.A., and McDonald, I. (2014) Precious and base metal geochemistry and mineralogy of the Grasvally norite-pyroxenite-anorthosite (GNPA) member, northern Bushveld Complex, South Africa: Implications for a multistage emplacement. Mineralium Deposita, 49, 667–692, https://doi.org/10.1007/s00126-014-0515-6.

Toulmin, P. III and Barton, P. Jr. (1964) A thermodynamic study of pyrite and pyrrhotite. Geochimica et Cosmochimica Acta, 28, 641–671, https://doi.org/10.1016/0016-7037(64)90083-3.

Trigub, A.L., Tagirov, B.R., Kvashnina, K.O., Chareev, D.A., Nickolsky, M.S., Shiryaev, A.A., Baranova, N.N., Kovalchuk, E.V., and Mokhov, A.V. (2017) X-ray spectroscopy study of the chemical state of "invisible" Au in synthetic minerals in the Fe-As-S system. American Mineralogist, 102, 1057–1065.

Zabinsky, S.I., Rehr, J.J., Ankudinov, A., Albers, R.C., and Eller, M.J. (1995) Multiple-scattering calculations of x-ray-absorption spectra. Physical Review B: Condensed Matter, 52, 2995–3009, https://doi.org/10.1103/PhysRevB.52.2995.

Manuscript received August 27, 2024
Manuscript accepted March 12, 2025
Accepted manuscript online March 19, 2025
Manuscript Handled by Fabrizio Nestola

Endnotes:

[1]Deposit item AM-25-119596. Online Materials are free to all readers. Go online, via the table of contents or article view, and find the tab or link for supplemental materials.